

# High-Speed Modulations of Guided Terahertz Waves via 2DEG Tiny Metasurfaces

Hongxin Zeng, Sen Gong, Lan Wang, Kesen Ding, Huajie Liang, Feng Lan, Tianchi Zhou, Shixiong Liang,\* Wei Wang, Yubin Gong, Ziqiang Yang, Tie Jun Cui, and Yaxin Zhang\*

Metasurfaces have emerged as fascinating planar optical components and devices, and, in particular, active metasurfaces confer more multifunctional expansions. However, the metasurface research has mainly focused on operating the light in free space, which hardly satisfies the system-level compactness and miniaturization. The potential of the metasurface for guided wave modulation remains to be further developed. Here, an integrated electronic device is reported by embedding a tiny metasurface, which consists of several patterned 2D electron gas (2DEG) microstructures in a waveguide. This device suppresses excessive parasitism to improve the modulation speed and enhances the electromagnetic field interaction to improve the modulation efficiency. It is experimentally demonstrated that high-speed modulations are electrically excited by the guided terahertz waves on a time scale of 40 ps via the tiny metasurface. This scheme represents a new platform for compact and high-speed integrated electronics.

characteristics.<sup>[7–11]</sup> The use of large-area dynamic materials on metasurfaces is an effective method to increase modulation bandwidth.<sup>[12–14]</sup> However, larger areas necessitate correspondingly larger excitation sources such as pumped light or complex feeder systems, which make miniaturization challenging while also introducing parasitic effects on modulation performance. Conversely, smaller areas require greater sensitivity of chosen dynamic material regions where it affects resonant  $Q$  most significantly. This requires careful design considerations like those seen in narrowband amplitude modulation achieved via embedding gate-controlled graphene blocks<sup>[15]</sup> or Complementary Metal Oxide Semiconductor (CMOS) transistors<sup>[16]</sup> into high- $Q$  metasurfaces. Based on this idea,

## 1. Introduction

Developing dynamic manipulation of terahertz (THz) electromagnetic signals has always been a long-term goal. From the early stage of terahertz technology development, the demand for high-speed, high-contrast, and high-efficient modulation was obvious.<sup>[1,2]</sup> Many researchers have been involved in this effort, and various outstanding achievements have been reported.<sup>[3–6]</sup> A common and valuable strategy is that the metasurface combines with electromagnetic resonance characteristics and the dynamic material with electromagnetic reconfigurable

various active metasurfaces for THz wave modulation have emerged employing doped silicon,<sup>[17–19]</sup> vanadium dioxide,<sup>[20–23]</sup> graphene,<sup>[24–27]</sup> high electron mobility transistor (HEMT),<sup>[28–30]</sup> liquid crystal,<sup>[31–33]</sup> and other dynamic materials.<sup>[34–36]</sup> The dielectric properties of these dynamic materials are usually adjusted by external pulsed lasers or electrical signals to reconstruct the resonant modes of active metasurfaces to modulate terahertz waves. The all-optical modulation strategy uses the strong interaction between pulsed laser and dynamic materials such as doped silicon,<sup>[12,22,37,38]</sup> lead iodide,<sup>[39]</sup> germanium oxide,<sup>[40,41]</sup> and vanadium oxide<sup>[13]</sup> to excite corresponding photogenerated


H. Zeng, S. Gong, L. Wang, K. Ding, F. Lan, T. Zhou, Y. Gong, Z. Yang, Y. Zhang  
Terahertz Communication Laboratory, School of Electronic Science and Engineering  
University of Electronic Science and Technology of China  
Chengdu 610000, China  
E-mail: zhangyaxin@uestc.edu.cn

H. Zeng, S. Gong, L. Wang, F. Lan, Z. Yang, T. J. Cui, Y. Zhang  
Terahertz Institute  
Zhangjiang National Laboratory  
Shanghai 201204, China

S. Gong, L. Wang, H. Liang, F. Lan, Z. Yang  
Yangtze Delta Region Institute (Huzhou)  
University of Electronic Science and Technology of China  
Huzhou 313000, China

S. Liang, W. Wang  
National Key Laboratory of Application Specific Integrated Circuit  
Hebei Semiconductor Research Institute  
Shijiazhuang 050000, China  
E-mail: liangsx@cetc13.cn

T. J. Cui  
Institute of Electromagnetic Space and State Key Laboratory of Millimeter Waves  
Southeast University  
Nanjing 210000, China

 The ORCID identification number(s) for the author(s) of this article can be found under <https://doi.org/10.1002/lpor.202300122>

© 2023 The Authors. Laser & Photonics Reviews published by Wiley-VCH GmbH. This is an open access article under the terms of the Creative Commons Attribution-NonCommercial-NoDerivs License, which permits use and distribution in any medium, provided the original work is properly cited, the use is non-commercial and no modifications or adaptations are made.

DOI: 10.1002/lpor.202300122

carriers on the metasurface to modulate terahertz wave in picosecond time scale. However, all-optical modulation relies on pulse laser as a modulation signal, which will cause thermal accumulation effect and degrade modulation performance after a long time of operation. In addition, pulsed laser emission equipment is usually large, which is difficult to achieve miniaturization and integration of application systems. The strategy of all-electric modulation uses all digital modulation signals, which can operate efficiently for a long time compared with all optical modulation, but its modulation speed still has a gap. To develop a higher electrical modulation speed, GaN-based 2D electron gas (2DEG) with high electron mobility, smaller resistance, and gate charge as the dynamic material in the metasurface for modulating the terahertz wave, which greatly improved the electrical modulation speed. A representative achievement is an optimized metasurface to effectively control the electron transport in buried 2DEG to suppress the parasitic effect and increase the modulation speed to 3 GHz.<sup>[28]</sup> Yet, this is still far lower than the typical modulation speed of the electro-optic modulator operating in near-infrared optical fiber.

One main reason for this gap lies in the fact that this modulation strategy usually depends on converting collective resonance modes of the large-area metasurfaces, which always suffers from an unavoidable parasitic effect. As we all know, the parasitic effect brings variation in electrical characteristics such as parasitic capacitance and inductance, especially the accumulation of parasitic capacitance limit on upper modulation speed.<sup>[9,42]</sup> In addition, the impedance matching of hundreds or thousands of units in a metasurface hinders the increase of modulation speed. During the large-scale preparation of dynamic components, it is difficult to ensure that the electrical performance of each dynamic component is consistent, which increases the parasitic parameters of the metasurface, making it difficult to calculate the matching impedance for broadband modulation signal. Traditional solutions always reduce the number of units on the metasurface to reduce parasitic effects, but this also decreases the coupling efficiency of spatial terahertz waves with the metasurface, declining the modulation depth. Meanwhile, such metasurface devices require normal or oblique incidence for the incoming THz wave in free space, which presents significant obstacles to system compactness.

Considering these concerns, more compact modulation strategies for guided waves have attracted the attention of researchers to reduce parasitic effects while ensuring coupling efficiency. The combination of ultrafast adjustability of graphene electromagnetic parameters with a terahertz waveguide opens a way for terahertz waveguide modulators.<sup>[43–45]</sup> Recently, the terahertz high-precision phase modulator implemented by the combination of guided wave and metaunit has successfully demonstrated the potential of the metaunits in the guided wave system.<sup>[46]</sup> Other guided wave modulation efforts depend on the optical switch,<sup>[47]</sup> which makes it less compatible with compact integration. Here, we describe a new approach to integrated metasurface-guided terahertz waves, which significantly suppresses the parasitic effect in the metasurface to improve the modulation speed. By combining the controllable transport of charge carriers within a 2DEG based on GaN HEMT with a tiny metasurface whose design is inspired by the earlier work on metasurface arrays, our device can simultaneously realize high modulation speed and high modula-

tion depth in a waveguide platform. After packaging, the device exhibits more than 16 GHz monophonic modulation speed, up to 94% modulation depth.

## 2. Results and Discussion

### 2.1. Structure and Design

Different from earlier work on metasurfaces, the proposed structure depicted in **Figure 1a** is not a collective resonant structure composed of a subwavelength array. Instead, it contains several microstructures nested with 2DEG nanostructures provided by GaN HEMT, which share the gate electrode, source electrode, and drain electrode, respectively. The schematic of the tiny metasurface is depicted in **Figure 1b**. The latticed metal metamaterial structure is prepared on a GaN layer, and a 160  $\mu\text{m}$  SiC layer acts as a substrate. The latticed metal metamaterial structure is composed of five dumbbell structures in series. The 3 nm 2DEG nanostructures induced from the spontaneous polarization and piezoelectric polarization effect of the AlGaIn/GaN heterostructure (25 nm  $\text{Al}_{0.27}\text{GaIn}_{0.73}$  barrier layer and a 1.5  $\mu\text{m}$  GaN layer) are buried in the gaps of the latticed metal metamaterial structure as dynamic switches. The two ends of the heterostructure are connected with the metal metamaterial by Ohmic contact to form the source and drain of HEMTs. The metal wire covering the center of the heterostructure forms a Schottky contact with HEMT as an electrical control gate. Therefore, the latticed metal metamaterial structure and several 2DEG nanostructures controlled by the gate together constitute the active tiny metasurface. The tiny metasurface is perpendicularly embedded in the rectangular waveguide ( $xy$  plane), stands in the waveguide cavity, and is parallel to the waveguide port. The microstrip line installed on the side wall of the rectangular waveguide is used as the modulation signal feed circuit. The gate electrode of the tiny metasurface is connected with the microstrip line for modulation signal loading, and the source–drain electrode links the inner wall of the waveguide via bond wires for ground connection. The fed terahertz waves propagate along the waveguide with  $\text{TE}_{10}$  mode and interact with the tiny metasurface to form a surface resonant mode. By applying diverse bias voltages, as shown in **Figure 1c**, the carrier concentration of the 2DEG is controlled to vary the interaction intensity between the terahertz waves and the tiny metasurface resulting in a high-speed modulation.

### 2.2. Modulation Principle

The modulation of the proposed device is based on the interaction between the  $\text{TE}_{10}$  mode in waveguide and the tiny 2DEG active metasurface, which is distinctively different from the traditional free space metasurface. To reveal the physics of the modulation, the instantaneous electromagnetic field of the entire structure is monitored and analyzed to extract persuasive information regarding the characteristics of electromagnetic interaction. The tiny metasurface is numerically simulated with a commercial software CST STUDIO SUITE. The tiny metasurface is placed on a SiC substrate with a relative permittivity of 9.8. In the simulation software, we use the classic Drude model

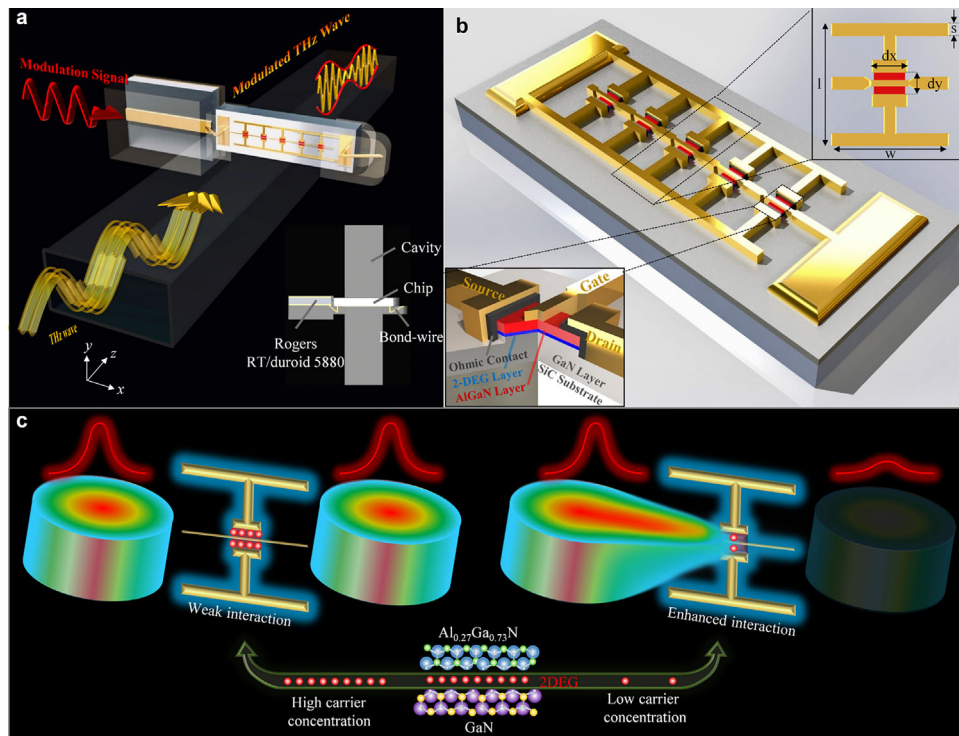


**Figure 1.** Device's architecture and its high-efficiency terahertz modulation. a) Schematic diagram of the overall structure. b) Schematic diagram of tiny metasurfaces and 2DEG nanostructures, and the relevant geometric parameters are as follows:  $s = 6 \mu\text{m}$ ,  $l = 140 \mu\text{m}$ ,  $w = 142 \mu\text{m}$ ,  $dx = 24 \mu\text{m}$ , and  $dy = 18 \mu\text{m}$ . c) Schematic diagram of modulation with different 2DEG concentrations. When the total gate electrode is unloaded with voltage, the carrier density is maintained at a high level in the 2DEG channel under the gap of the source and drain. The interaction of the terahertz wave  $\text{TE}_{10}$  mode with the surface resonance mode is weak and hardly affects the transmission. When the total gate electrode is loaded with negative voltage, the carrier density decreases in the 2DEG channel, and the electron-transport path at the gap of the source and drain is pinch-off, showing a strong interaction with the terahertz wave, destroying the waveguide  $\text{TE}_{10}$  mode.

to characterize the electron-transport characteristics of 2DEG with different carrier concentrations. The equivalent permittivity is expressed as follows

$$\epsilon(\omega) = \epsilon_{\infty} + i\omega_p^2 \frac{\gamma\omega^{-1}}{\omega^2 + \gamma^2} \quad (1)$$

The real part of the equivalent permittivity  $\epsilon_{\infty}$  is equal to the relative permittivity of GaN ( $\epsilon_{\infty} = 9.8$ ). In the imaginary part,  $\omega_p^2 = e^2 N_s / \epsilon_0 m^* d$  is the plasma frequency,  $\gamma = 2\pi \times 1.4$  is the collision frequency, which is calculated with the relation  $\gamma = e/m^* \mu$ . Where  $\mu$ ,  $e$ , and  $m^*$  are the electron mobility of the channel, the electron charge, and effective mass, respectively. For the expression of plasma frequency,  $N_s$  is the 2D carrier concentration and  $d$  is the thickness of the channel layer. Therefore, we can equivalently simulate the process of depleting the 2DEG from the actual applied gate voltage by changing the value of  $\omega_p$ .

The modulation process is mainly composed of two states: high-transmission state and low-transmission state. In the high-transmission state, the interaction between the terahertz wave and metasurface is weak, and the  $\text{TE}_{10}$  mode of guided terahertz wave transmits the metasurface. In the low-transmission state, terahertz wave interacts with the metasurface, and the guided wave  $\text{TE}_{10}$  mode is converted to the surface dipole resonant mode

of the metasurface, which hinders the transmission of terahertz wave. The electromagnetic field induced by metasurface dipole resonance is reversed from the accompanying electromagnetic field, which weakens the incident accompanying electric field and magnetic field intensity, disrupting the  $\text{TE}_{10}$  mode transmitted within the waveguide and preventing electromagnetic waves from propagating forward. Traditional metasurfaces are mainly realized by the principle of electric field cancellation. The magnetic field in free space is parallel to the metasurface, and it is difficult to eliminate the circular magnetic field induced by the metasurface.<sup>[28–30]</sup> The circular magnetic field of  $\text{TE}_{10}$  mode propagated by the waveguide can further enhance the magnetic field cancellation effect to prevent more electromagnetic wave transmission. As shown in **Figure 2a**, for the fed terahertz waves, its electric field vector is along the  $y$ -axis, and the magnetic field vector is distributed in a ring. For example, when the incident electric field vector is in the  $-\gamma$  direction, the accompanied magnetic fields form a counterclockwise ring in the  $xz$  plane. Induced by the incident electric field, an induced current is caused along the  $-\gamma$  direction in the dumbbell microstructure, which induces a clockwise magnetic field near the structure, as shown in **Figure 2b**. This reverse magnetic field behavior shows that induced electromagnetic metasurface can destroy  $\text{TE}_{10}$  electromagnetic mode and prevent terahertz guided wave from propagating forward.

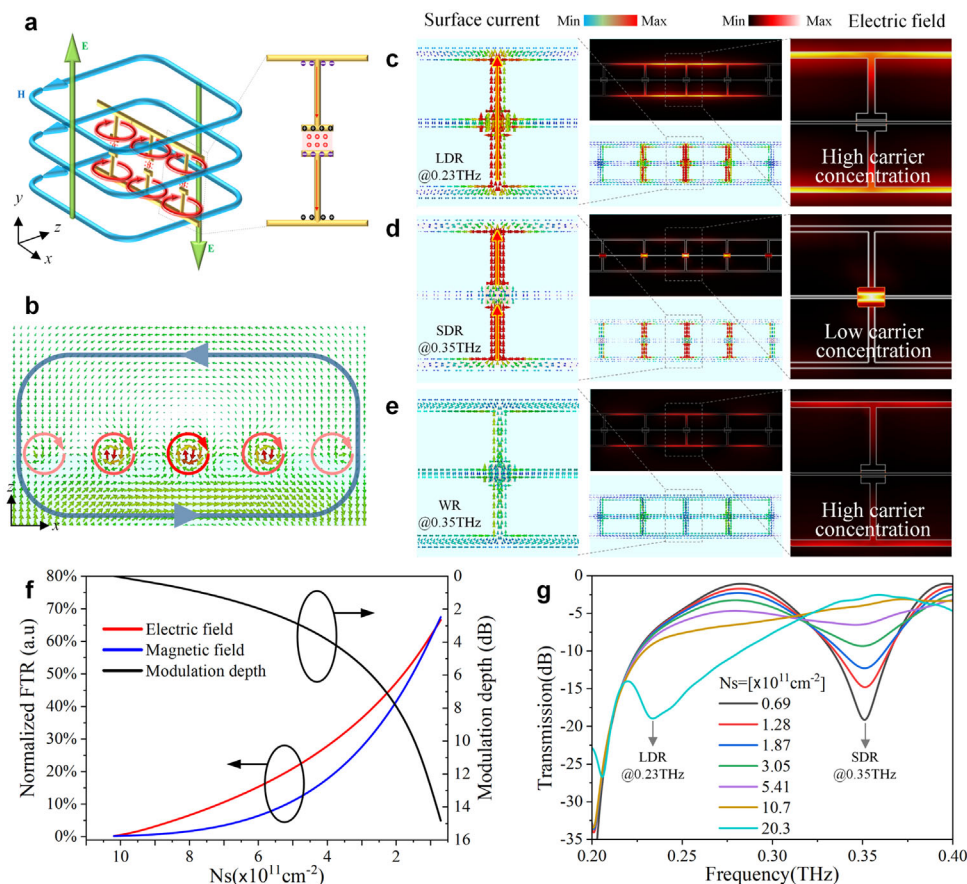


**Figure 2.** Electromagnetic simulation results are calculated by the commercial simulation software CST Studio Suite. a) Schematic diagram of electromagnetic interaction. The accumulated positive (black ball) and negative charges (purple ball) at the ends of the gap on the tiny metasurface. b) Magnetic field distribution of tiny metasurfaces in the  $xy$  plane. The surface current distribution of tiny metasurfaces under high carrier concentration. c) The surface current and electric field distribution during long dipole resonance. d) The surface current and electric field distribution during short dipole resonance. e) The surface current and electric field distribution during weak resonance. f) Normalized electric and magnetic field tuning ratio (FTR, the ratio of the electric field or magnetic field intensity normalized by its maximum field value, respectively) and modulation depth as a function of 2DEG carrier concentrations. The electromagnetic field intensity and modulation depth are normalized with the maximum carrier concentration. g) Transmission as a function of frequency.

This can be confirmed further by the details of the progress. In high-carrier-concentration scenarios, electrons move smoothly through the electron channel and oscillate throughout the central line forming a long dipole resonance (LDR) with a resonance frequency at 0.23 THz, as shown in Figure 2c. This results in less electron accumulation in source and drain regions with field concentrated at edges of the metasurface, while surface current shows a uniform distribution. On the other hand, the low carrier concentration leads to electron channel pinch-off, which prevents the free electrons from moving around the microstructure and causes the central long line to split into two short lines. This suppresses the LDR while inducing a new bipolar short dipole resonance (SDR) as observed in Figure 2d with a resonance frequency point of 0.35 THz. Electrons gather at the source and drain to form a powerful induced electric field and induced current. The electric fields are mainly concentrated in the gaps of the dumbbell-shaped microstructure, and the electric field distribution is weak in other regions. This indicates that the additional parasitic capacitance is reduced and weakens the parasitic effects caused by the electromagnetic coupling between

the microstructures in the normal metasurface. By changing the concentration of 2DEG carriers in the gaps, the resonant modes can be switched between LDR and SDR, resulting in frequency shifts of the resonant peaks from 0.23 to 0.35 THz. At high electron concentrations, as shown in Figure 2e, the metasurface is unable to interact with electromagnetic waves near 0.35 THz, and the induced electric fields at the source and drain electrodes, as well as the induced current on the metal arm, are not significant, forming a weak resonance (WR). In addition, to further elucidate the impact of this electromagnetic mechanism on modulation depth, we extracted the electric and magnetic field intensities near the microstructure at different 2DEG concentrations. As shown in Figure 2f, as the concentration of 2DEG carriers decreases, the induced electric and magnetic field strengths increase and the field tuning ratio (FTR) reaches nearly 70%. As the induced electromagnetic field increases, the modulation depth gradually increases from 0 to 15 dB (equivalent to 93%). Therefore, the intensity of the induced electromagnetic field can be changed to modulate terahertz waves by changing the concentration of 2DEG carriers. The simulated

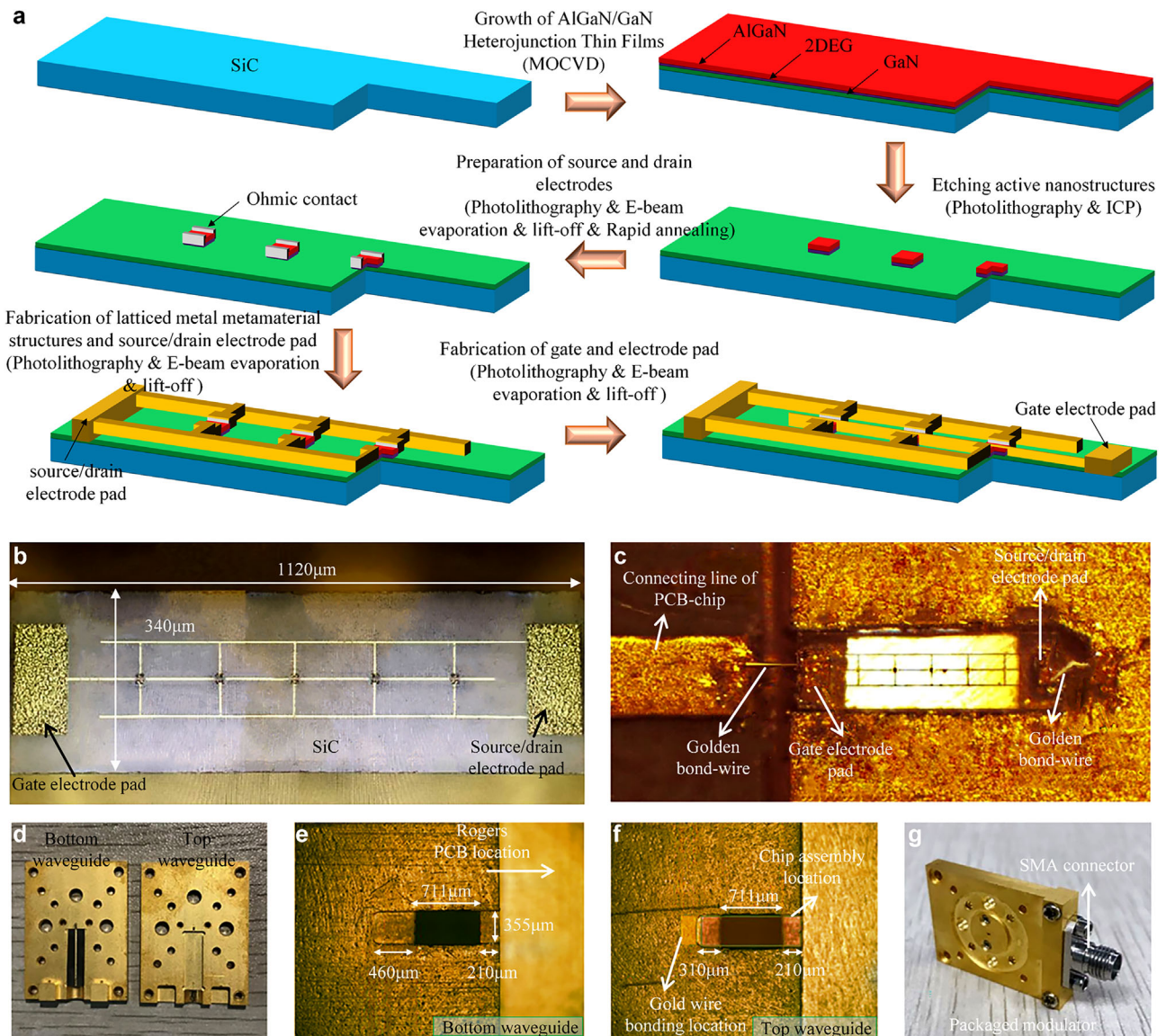


**Figure 3.** The preparation process and the packaging of the tiny metasurface. a) Process flow for the fabrication of tiny metasurface embedded with the nanostructured 2DEG layer. b) Microscope photograph of tiny metasurface. c) The assembled tiny metasurface. d) Top and bottom waveguides before assembly. e, f) The top and bottom waveguide slots for placing tiny metasurfaces, respectively. g) Overall structure of packaged modulator.

terahertz wave transmission spectrum (Figure 2g) indicates that the electromagnetic induction effect of the embedded waveguide tiny metasurface leads to significant amplitude modulation. When the electron concentration remains at high concentrations of  $20.3 \times 10^{11} \text{ cm}^{-2}$ , significant resonance characteristics (LDR) appear in the low-frequency range. As the carrier concentration gradually decreases to  $0.65 \times 10^{11} \text{ cm}^{-2}$ , the resonant frequency shifted to around 0.35 THz, and a maximum modulation depth of 15 dB was obtained at that frequency.

### 2.3. Processing and Assembly

We adopt micro–nano processing technology to prepare the tiny metasurface. The manufacturing process is mainly divided into

the following steps, as shown in Figure 3a. First of all, the metal–organic chemical vapor deposition (MOCVD) method is used to grow AlGaIn (25 nm)/GaIn (1.5 μm) heterojunction films on a 150 μm SiC substrate. Next, a positive photoresist layer with a thickness of 1.2 μm is spin-coated on the AlGaIn film, and the active region of 2DEG is limited by photolithographic development using a mask. The AlGaIn film outside the active region is overetched using an inductively coupled plasma (ICP) mixed with Cl<sub>2</sub>-BCl<sub>3</sub> to obtain a 2DEG nanostructure with a thickness of 25 nm. Ti/Al/Ni/Au (20 nm/120 nm/70 nm/100 nm) composite metal layers were successively deposited at both ends of the active region as source and drain electrodes through photolithography, electron beam evaporation, and stripping processes. The source electrode and drain electrode form Ohmic contact with 2DEG by rapid annealing (100 s) from 900 °C to room temperature in an

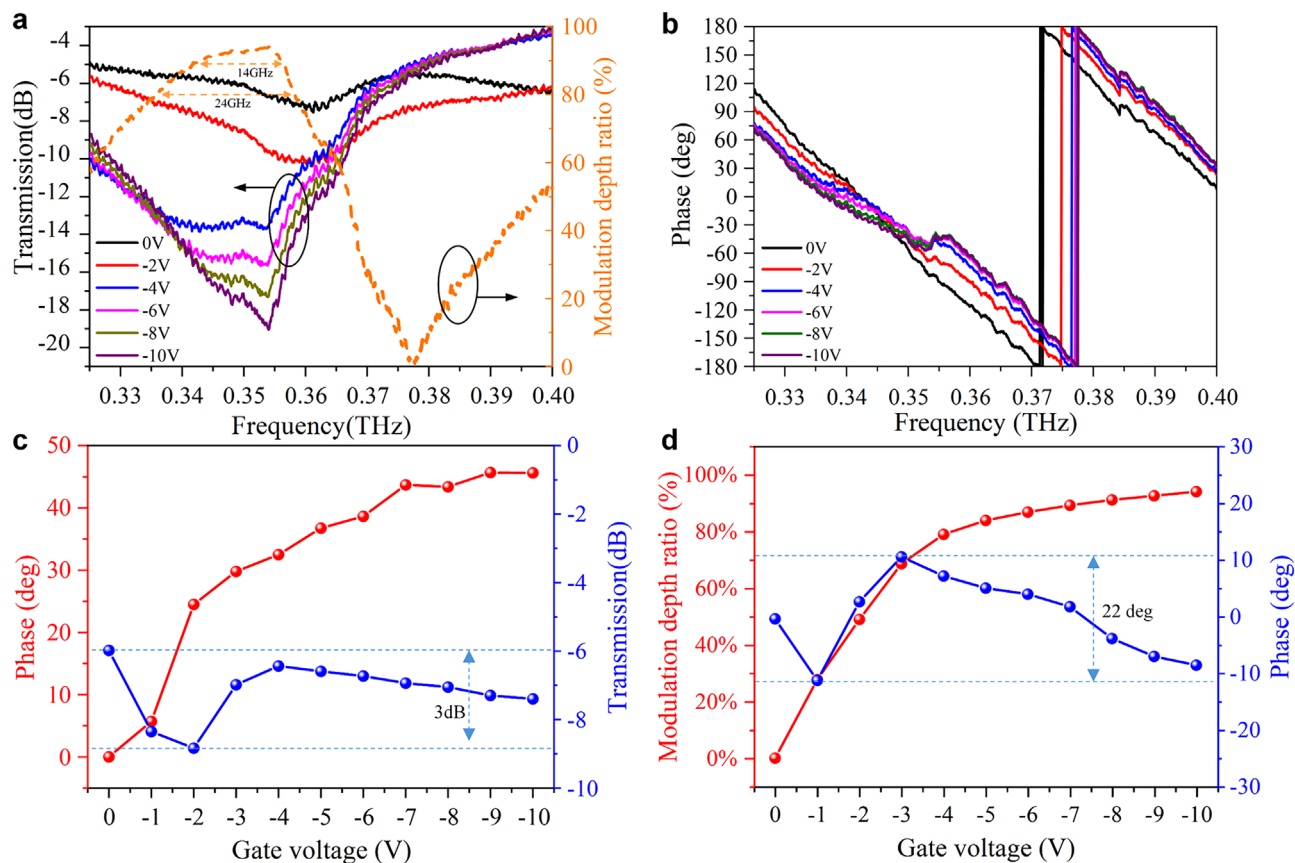


**Figure 4.** Experimental measurement results of prototype device. The scattering parameters of the two-port network are measured by changing the DC power supply voltage (from 0 to  $-10$  V). a) Transmission and modulation depth ratio for different gate voltages. b) Transmitted phase for different gate voltages. c) Phase modulation and transmission amplitude fluctuation. d) Modulation depth ratio and time fluctuation.

environment full of nitrogen. Using similar photolithography, electron beam evaporation, and stripping processes, a 200 nm gold layer with a 50 nm nickel adhesive layer is deposited on the GaN layer to form a latticed metal metamaterial structure and source/drain electrode pad. Finally, precision electron beam lithography fabricated Au/Ni (150 nm/50 nm) gates. The manufactured tiny metasurface is shown in Figure 3b. The length of this metasurface is 1112  $\mu\text{m}$  and the width is 340  $\mu\text{m}$ . In order to reduce the contact resistance of the bonding wires, both total electrodes on the metasurface were treated with rapid thermal annealing treatment to make the electrode pads form Ohmic contact with the substrate. Figure 3c is the assembly diagram of tiny metasurface and microstrip line. The gate general electrode on the tiny metasurface is connected with the central wire of the microstrip line through two bonding wires, and the two gold wires connecting the source and drain general electrodes are bonded on the side of the waveguide wall. This metasurface was packaged in a metallic cavity composed of a top waveguide and a bottom waveguide (Figure 3d). The inner surface of the bottom waveguide is provided with slots for assembled tiny metasurface and microstrip lines (Figure 3e). The top waveguide is also grooved at the position corresponding to the tiny metasurface and the microstrip line to convenient the assembly of gold wire bonding and SubMiniature version A (SMA) connector probes (Figure 3f). The complete prototype device is assembled from the top and bottom

waveguides (Figure 3g). The SMA adapter is fixed on the side-wall of the waveguide, and the central probe of the coaxial line is connected to the central wire of the microstrip line for feeding in external modulation signals.

#### 2.4. Experimental Results

To characterize the modulation spectrum characteristics of the device, the frequency domain spectrum is measured using a THz vector network analyzer (VNA, AV3672B). The VNA used in the experiment covers the frequency range from 10 MHz to 26.5 GHz. After the external spread spectrum module (AV3649B) is connected, the spectrum measure range is increased covering 0.325–0.50 THz to meet the measure requirements. The input and output ports of the device are standard rectangular waveguides, which are, respectively, connected to the spread spectrum module, and DC voltage is applied to the device through the SMA connector. We define the modulation depth ratio as  $T_{-10V} - T_{0V} / T_{-10V} \times 100\%$  to characterize the modulation effect of the device, where  $T_{-10V}$  and  $T_{0V}$  are the transmission under the gate voltages of  $-10$  and  $0$  V, respectively. The transmission spectra and modulation depth ratio results for different DC gate voltages are shown in Figure 4a. Under zero gate voltage, the transmission spectrum is flat without obvious resonances. With

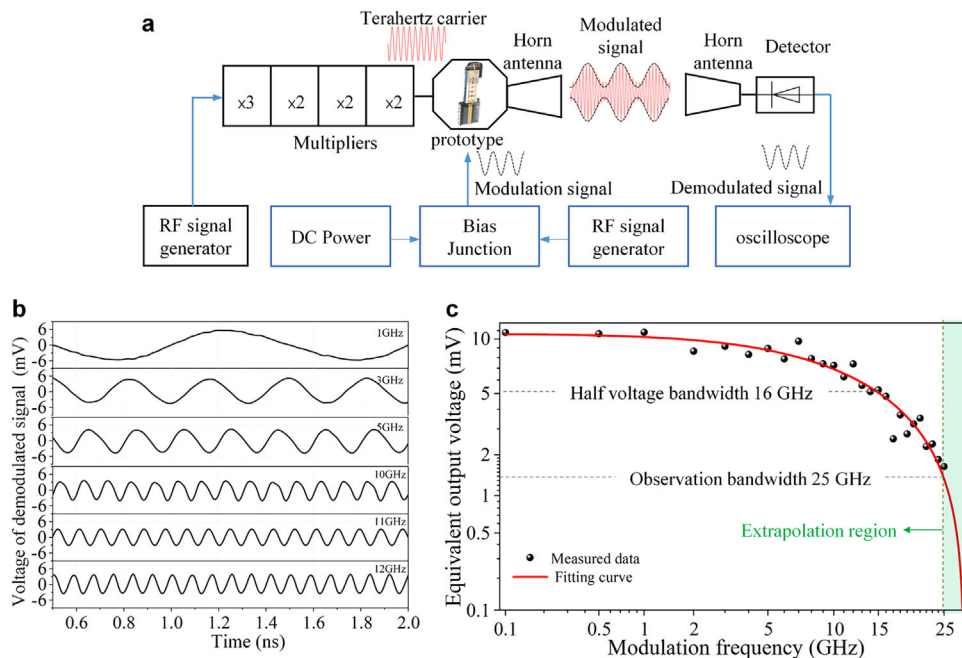


**Figure 5.** Modulation speed experiment. a) Experimental block diagram of the modulation speed system. b) Demodulation waveforms of different tone modulation signals in the oscilloscope. c) Function of demodulation frequency and equivalent output voltage.

the increase of gate voltage, 2DEG channel is gradually blocked, and an obvious resonant peak appears near 0.35 THz. The 2DEG is completely depleted at  $\approx -10$  V with a 94% modulation depth ratio at 0.354 THz (Figure 4a, yellow dotted line). It is worth noting that the operating bandwidths with modulation depth ratios above 90% and 80% are 14 and 24 GHz, respectively. In addition to amplitude modulation, phase modulation is demonstrated in Figure 4b. The variations of carrier concentration in the 2DEG lead to corresponding changes the electron motion time in the tiny metasurface, exhibiting terahertz wave overshoot and lag. The electrons take some time to aggregate between the channels, causing the terahertz wave to exhibit phase lag. As shown in Figure 4c, the amount of phase lag gradually increases to  $45^\circ$  with the gate voltage increasing from 0 to  $-10$  V, while the amplitude changes stay within 3 dB. A low-transmission amplitude fluctuation is maintained while phasing modulation. On the other hand, as shown in Figure 4d, amplitude modulation needs to suppress unnecessary phase modulation. The experimental results show that 90% of the modulation depth ratio has only  $22^\circ$  of phase fluctuation, effectively ensuring terahertz amplitude modulation stability.

Next, a modulation speed experiment is performed to demonstrate the real-time modulation characteristics further. The modulation speed measurement system is composed of three key components: THz generator, THz device, and THz receiver. The system block diagram is shown in Figure 5a. The terahertz wave is generated by the radio frequency (RF) signal generator after a frequency tripler and three frequency doublers. The device is directly connected to the last-stage frequency doubler to modulate the input terahertz carrier signal. The measured modulation signal is provided by an RF signal generator (1–25 GHz) and loaded into the device after the bias connector to complete high-speed modulation. The modulated signal is radiated to free

space from the transmitting horn antenna (gain: 25 dBi). The reception of the signal adopts the direct detector receiving scheme. The receiving antenna captures the modulated signal of space propagation to the THz high-speed detector (WR2.8ZBD-F, Virginia Diodes Inc.) to detect the envelope of the modulated signal and output the demodulated signal. The measurement results for modulation frequencies of 1–12 GHz (the corresponding time scale is 83–1000 ps) are shown in Figure 5b. If the modulation speed is slower than the time scale of the loaded sinusoidal signal, the response time displayed on the oscilloscope causes severe signal distortion. This phenomenon does not occur in this device from 1 to 12 GHz, and all demodulated signals are standard sinusoidal waveforms. However, the demodulated waveform of higher speed cannot be displayed correctly because the experimental oscilloscope's bandwidth and sampling speed cannot meet the acquisition of signals larger than 12 GHz. Therefore, a spectrum analyzer with a broader response frequency (response bandwidth: 25 GHz) is employed to perform a spectrum measure of the demodulated signal and convert it into an equivalent output level according to the output power. As shown in Figure 5c, it can be found that the measured half-voltage drop bandwidth is 16 GHz. In addition, the valid output level can be detected in the entire spectrum analyzer bandwidth, with a minimum level of 1.5 mV at 25 GHz, corresponding to a time scale of 40 ps.

Benefitting from the properties of parasitism suppression, the waveguide-embedded tiny metasurface exhibits fast modulation performance, almost one or several orders of magnitude higher than the conventional metasurface.<sup>[28,29]</sup> In addition, a small number of microstructures are beneficial to the impedance matching of the modulation signal, making it easier to load the high-speed modulation signal onto the metasurface, especially if the modulation speed is beyond GHz. With the increase in modulation signal speed, the loss loaded on the device increases,

resulting in the decreased amplitude of the received demodulated signal. This issue will be solved in the follow-up technical work, such as replacing the existing SMA with a higher cutoff frequency coaxial and applying a heterogeneous integration technique to integrate the modulation signal feed circuit and the tiny metasurface on a single chip. Nonetheless, the excellent guided wave modulation has experimentally been demonstrated, verifying the advantages of the tiny metasurface and guiding wave electromagnetic interaction mechanism and significantly improving the direct modulation speed.

### 3. Conclusion

In summary, we experimentally demonstrate high-speed modulation for guided terahertz waves via a tiny metasurface. This strategy exhibits strong parasitism suppression properties, high speed modulating with electrically excited on a time scale of 40 ps. This work has great potential for terahertz device or system applications. For example, combine the metasurface with different resonant characteristics and waveguide multiplexer to select the signal channel to achieve high-speed time-division or frequency-division communication. Furthermore, combined with a multi-channel concept achieves higher order and more dimensional terahertz modulation. This combination of waveguide and metasurface has a qualitative leap for terahertz modulation and provides a new platform for terahertz-integrated systems.

### Acknowledgements

H.Z. and S.G. contributed equally for this work. This work was supported by the National Key Research and Development Program of China (Program Nos. 2018YFB1801503 and 2021YFA1401000), the National Natural Science Foundation of China (Grant Nos. 62101111, 61931006, 62131007, U20A20212, 61901093, 61871419, and 61921002), the Sichuan Province Science and Technology Support Program under Contract No.2020JRC0028, the Fundamental Research Funds for the Central Universities (Grant No. ZYGX2020ZB011), and the China Postdoctoral Science Foundation (Grant No. 2020M683285).

### Conflict of Interest

The authors declare no conflict of interest.

### Data Availability Statement

The data that support the findings of this study are available from the corresponding author upon reasonable request.

### Keywords

guided waves, metasurfaces, modulation, terahertz

Received: February 9, 2023

Revised: June 1, 2023

Published online:

[1] T. Kleine-Ostmann, T. Nagatsuma, *J. Infrared Milli. Terahz. Waves* **2011**, *32*, 143.

- [2] J. Federici, L. Moeller, *J. Appl. Phys.* **2010**, *107*, 111101.
- [3] A. Dunn, C. Poysier, P. Dean, A. Demić, A. Valavanis, D. Indjin, M. Salihi, I. Kundu, L. Li, A. Akimov, A. G. Davies, E. Linfield, J. Cunningham, A. Kent, *Nat. Commun.* **2020**, *11*, 835.
- [4] K. Sengupta, T. Nagatsuma, D. M. Mittleman, *Nat. Electron.* **2018**, *1*, 622.
- [5] B. Sensale-Rodriguez, R. Yan, M. M. Kelly, T. Fang, K. Tahy, W. S. Hwang, D. Jena, L. Liu, H. G. Xing, *Nat. Commun.* **2012**, *3*, 780.
- [6] H. Zeng, S. Gong, L. Wang, T. Zhou, Y. Zhang, F. Lan, X. Cong, L. Wang, T. Song, Y. Zhao, Z. Yang, D. M. Mittleman, *Nanophotonics* **2022**, *11*, 415.
- [7] H.-T. Chen, W. J. Padilla, M. J. Cich, A. K. Azad, R. D. Averitt, A. J. Taylor, *Nat. Photonics* **2009**, *3*, 148.
- [8] W. L. Chan, H.-T. Chen, A. J. Taylor, I. Brener, M. J. Cich, D. M. Mittleman, *Appl. Phys. Lett.* **2009**, *94*, 213511.
- [9] H.-T. Chen, W. J. Padilla, J. M. O. Zide, A. C. Gossard, A. J. Taylor, R. D. Averitt, *Nature* **2006**, *444*, 597.
- [10] Y. Zhao, Y. Zhang, Q. Shi, S. Liang, W. Huang, W. Kou, Z. Yang, *ACS Photonics* **2018**, *5*, 3040.
- [11] M. Manjappa, P. Pitchappa, N. Singh, N. Wang, N. I. Zheludev, C. Lee, R. Singh, *Nat. Commun.* **2018**, *9*, 4056.
- [12] Y. Huang, K. Kaj, C. Chen, Z. Yang, S. R. Ul Haque, Y. Zhang, X. Zhao, R. D. Averitt, X. Zhang, *ACS Photonics* **2022**, *9*, 1150.
- [13] X. Zhao, J. Lou, X. Xu, Y. Yu, G. Wang, J. Qi, L. Zeng, J. He, J. Liang, Y. Huang, D. Zhang, C. Chang, *Adv. Opt. Mater.* **2022**, *10*, 2102589.
- [14] A. Di Gaspare, E. A. A. Pogna, E. Riccardi, S. M. A. Sarfraz, G. Scamarcio, M. S. Vitiello, *Adv. Opt. Mater.* **2022**, *10*, 2200819.
- [15] A. M. Zaman, Y. Lu, X. Romain, N. W. Almond, O. J. Burton, J. Alexander-Webber, S. Hofmann, T. Mitchell, J. D. P. Griffiths, H. E. Beere, D. A. Ritchie, R. Degl'Innocenti, *IEEE Trans. Terahertz Sci. Technol.* **2022**, *12*, 520.
- [16] S. Venkatesh, X. Lu, H. Saeidi, K. Sengupta, *Nat. Electron.* **2020**, *3*, 785.
- [17] L. Ding, X. Luo, L. Cheng, M. Thway, J. Song, S. J. Chua, E. E. M. Chia, J. Teng, *Adv. Opt. Mater.* **2018**, *6*, 1800928.
- [18] L. Deng, J. Teng, H. Liu, Q. Y. Wu, J. Tang, X. Zhang, S. A. Maier, K. P. Lim, C. Y. Ngo, S. F. Yoon, S. J. Chua, *Adv. Opt. Mater.* **2013**, *1*, 128.
- [19] N.-H. Shen, M. Massaouti, M. Gokkavas, J.-M. Manceau, E. Ozbay, M. Kafesaki, T. Koschny, S. Tzortzakis, C. M. Soukoulis, *Phys. Rev. Lett.* **2011**, *106*, 037403.
- [20] W. Kou, W. Shi, Y. Zhang, Z. Yang, T. Chen, J. Gu, X. Zhang, Q. Shi, S. Liang, F. Lan, H. Zeng, Z. Yang, *IEEE Trans. Terahertz Sci. Technol.* **2021**, *1*, 13.
- [21] X. Liu, Q. Wang, X. Zhang, H. Li, Q. Xu, Y. Xu, X. Chen, S. Li, M. Liu, Z. Tian, C. Zhang, C. Zou, J. Han, W. Zhang, *Adv. Opt. Mater.* **2019**, *7*, 1900175.
- [22] L. Cong, Y. K. Srivastava, H. Zhang, X. Zhang, J. Han, R. Singh, *Light: Sci. Appl.* **2018**, *7*, 28.
- [23] M. Liu, H. Y. Hwang, H. Tao, A. C. Strikwerda, K. Fan, G. R. Keiser, A. J. Sternbach, K. G. West, S. Kittiwatanakul, J. Lu, S. A. Wolf, F. G. Omenetto, X. Zhang, K. A. Nelson, R. D. Averitt, *Nature* **2012**, *487*, 345.
- [24] T. Ye, B. Wang, C. Wang, Z. Li, Z. Zhang, K. Jin, L. Wang, Y. Yin, *Adv. Opt. Mater.* **2019**, *7*, 1900315.
- [25] A. Ahmadvand, B. Gerislioglu, Z. Ramezani, *Nanoscale* **2019**, *11*, 8091.
- [26] S. Arezoomandan, K. Yang, B. Sensale-Rodriguez, *Appl. Phys. A* **2014**, *117*, 423.
- [27] S. H. Lee, M. Choi, T.-T. Kim, S. Lee, M. Liu, X. Yin, H. K. Choi, S. S. Lee, C.-G. Choi, S.-Y. Choi, X. Zhang, B. Min, *Nat. Mater.* **2012**, *11*, 936.
- [28] Y. Zhao, L. Wang, Y. Zhang, S. Qiao, S. Liang, T. Zhou, X. Zhang, X. Guo, Z. Feng, F. Lan, Z. Chen, X. Yang, Z. Yang, *Nano Lett.* **2019**, *19*, 7588.



- [29] Y. Zhang, S. Qiao, S. Liang, Z. Wu, Z. Yang, Z. Feng, H. Sun, Y. Zhou, L. Sun, Z. Chen, X. Zou, B. Zhang, J. Hu, S. Li, Q. Chen, L. Li, G. Xu, Y. Zhao, S. Liu, *Nano Lett.* **2015**, *15*, 3501.
- [30] Y. Zhang, Y. Zhao, S. Liang, B. Zhang, L. Wang, T. Zhou, W. Kou, F. Lan, H. Zeng, J. Han, Z. Feng, Q. Chen, P. Mazumder, Z. Yang, *Nanophotonics* **2019**, *8*, 153.
- [31] M. Bosch, M. R. Shcherbakov, K. Won, H.-S. Lee, Y. Kim, G. Shvets, *Nano Lett.* **2021**, *21*, 3849.
- [32] J. Wu, Z. Shen, S. Ge, B. Chen, Z. Shen, T. Wang, C. Zhang, W. Hu, K. Fan, W. Padilla, Y. Lu, B. Jin, J. Chen, P. Wu, *Appl. Phys. Lett.* **2020**, *116*, 131104.
- [33] L. Wang, X.-W. Lin, W. Hu, G.-H. Shao, P. Chen, L.-J. Liang, B.-B. Jin, P.-H. Wu, H. Qian, Y.-N. Lu, X. Liang, Z.-G. Zheng, Y.-Q. Lu, *Light: Sci. Appl.* **2015**, *4*, e253.
- [34] Y. K. Srivastava, M. Manjappa, L. Cong, H. N. S. Krishnamoorthy, V. Savinov, P. Pitchappa, R. Singh, *Adv. Mater.* **2018**, *30*, 1801257.
- [35] C. Li, J. Wu, S. Jiang, R. Su, C. Zhang, C. Jiang, G. Zhou, B. Jin, L. Kang, W. Xu, J. Chen, P. Wu, *Appl. Phys. Lett.* **2017**, *111*, 092601.
- [36] S. Chen, F. Fan, Y. Miao, X. He, K. Zhang, S. Chang, *Nanoscale* **2016**, *8*, 4713.
- [37] Q. Zhou, Y. Li, T. Wu, Q. Qiu, J. Duan, L. Jiang, W. Mao, N. Yao, Z. Huang, *Laser Photonics Rev.* **2023**, *17*, 2200808.
- [38] J. Lou, J. Liang, Y. Yu, H. Ma, R. Yang, Y. Fan, G. Wang, T. Cai, *Adv. Opt. Mater.* **2020**, *8*, 2000449.
- [39] M. Manjappa, A. Solanki, A. Kumar, T. C. Sum, R. Singh, *Adv. Mater.* **2019**, *31*, 1901455.
- [40] T. C. Tan, Y. K. Srivastava, R. T. Ako, W. Wang, M. Bhaskaran, S. Sriram, I. Al-Naib, E. Plum, R. Singh, *Adv. Mater.* **2021**, *33*, 2100836.
- [41] P. Pitchappa, A. Kumar, S. Prakash, H. Jani, R. Medwal, M. Mishra, R. S. Rawat, T. Venkatesan, N. Wang, R. Singh, *Adv. Funct. Mater.* **2021**, *31*, 2100200.
- [42] P. Q. Liu, I. J. Luxmoore, S. A. Mikhailov, N. A. Savostianova, F. Valmorra, J. Faist, G. R. Nash, *Nat. Commun.* **2015**, *6*, 8969.
- [43] I. Khromova, A. Andryieuski, A. Lavrinenko, *Laser Photonics Rev.* **2014**, *8*, 916.
- [44] A. Locatelli, G. E. Town, C. De Angelis, *IEEE Trans. Terahertz Sci. Technol.* **2015**, *5*, 351.
- [45] M. Mittendorff, S. Li, T. E. Murphy, *ACS Photonics* **2017**, *4*, 316.
- [46] H. Zeng, H. Liang, Y. Zhang, L. Wang, S. Liang, S. Gong, Z. Li, Z. Yang, X. Zhang, F. Lan, Z. Feng, Y. Gong, Z. Yang, D. M. Mittleman, *Nat. Photonics* **2021**, *15*, 751.
- [47] T. Sjørgård, T. Hawkins, J. Ballato, U. L. Österberg, U. J. Gibson, *Opt. Express* **2021**, *29*, 3543.